



# **JGR Space Physics**

# RESEARCH ARTICLE

10.1029/2019JA027664

#### **Key Points:**

- A period of almost purely radial interplanetary magnetic field (IMF) (cone angle < 3°) was embedded in the radial IMF event for January 4, 2014
- IMF B<sub>y</sub> or B<sub>z</sub> related polewardmoving aurora was created by precipitating electrons along the open field lines in the cusp during the period
- The antisunward ionospheric convection became stable and consistent with magnetometer observations when the IMF was almost purely radial

#### **Supporting Information:**

Supporting Information may be found in the online version of this article.

#### Correspondence to:

J. H. Shue, jhshue@jupiter.ss.ncu.edu.tw

# Citation:

Li, H.-M., Shue, J.-H., Taguchi, S., Nosé, M., Hosokawa, K., Ruohoniemi, J. M., et al. (2021). Dayside cusp aurorae and ionospheric convection under radial interplanetary magnetic fields. *Journal of Geophysical Research: Space Physics*, 126, e2019JA027664. https://doi.org/10.1029/2019JA027664

Received 21 NOV 2019 Accepted 23 APR 2021

# Dayside Cusp Aurorae and Ionospheric Convection Under Radial Interplanetary Magnetic Fields

Hsien-Ming Li<sup>1</sup>, Jih-Hong Shue<sup>1</sup>, Satoshi Taguchi<sup>2</sup>, Masahito Nosé<sup>3</sup>, Keisuke Hosokawa<sup>4</sup>, J. Michael Ruohoniemi<sup>5</sup>, Yongliang Zhang<sup>6</sup>, Simon Wing<sup>6</sup>, and Mark Lester<sup>7</sup>

<sup>1</sup>Institute of Space Science, National Central University, Taoyuan, Taiwan, R.O.C, <sup>2</sup>Department of Geophysics, Graduate School of Science, Kyoto University, Kyoto, Japan, <sup>3</sup>Institute for Space-Earth Environmental Research, Nagoya University, Nagoya, Japan, <sup>4</sup>Department of Communication Engineering and Informatics, University of Electro-Communications, Chofu, Japan, <sup>5</sup>Bradley Department of Electrical and Computer Engineering, Virginia Tech, Blacksburg, VA, USA, <sup>6</sup>The Johns Hopkins University Applied Physics Laboratory, Laurel, MD, USA, <sup>7</sup>Department of Physics and Astronomy, University of Leicester, Leicester, UK

**Abstract** Dayside cusp aurorae are created from particles precipitating into the cusp, and ionospheric convection is driven by solar wind electric fields. In this study, we coordinated the observations obtained from the all-sky camera on Svalbard, the Super Dual Auroral Radar Network, SuperMAG magnetometer data, and far ultraviolet imagers on board the Defense Meteorological Satellite Program satellites for the event January 4, 2014 to examine the morphology of aurorae and the patterns of ionospheric convection for radial interplanetary magnetic field (IMF). During the event, a poleward-moving auroral form and antisunward ionospheric convection were observed when the IMF turned into almost purely radial. Moreover, both types of antisunward and sunward convection were simultaneously observed near the footprint of the cusp at different times during the radial IMF period. The antisunward convection and sunward convection are typically an indicator of the dayside reconnection for the southward IMF and the lobe reconnection for the northward IMF, respectively. All those observations support the concept of low-latitude dayside and high-latitude lobe reconnection for the radial IMF. This study further shows that the coexistence of the two types of reconnection for radial IMF, resulting in an interplay of repetitive antisunward and sunward convection.

**Plain Language Summary** The event for January 4, 2014 enables us to study the features of dayside cusp aurorae and ionospheric convection for the radial IMF. During the event, a poleward-moving auroral form and antisunward convection were observed near the footprint of the cusp, which provides indirect evidence of the magnetic reconnection that occurs at the dayside magnetopause for the radial IMF. S-shaped aurorae, named from their morphology, near the cusp were also observed during the event. This type of aurora was possibly created by magnetosheath plasma jets impinging on the surface of the magnetopause or magnetic reconnection occurring locally on the magnetopause. For ionospheric convection, the primary convection pattern for the radial IMF was similar to that for the southward IMF, particularly for antisunward convection near the cusp. However, sunward convection near the cusp was also observed at the same time, indicating the lobe reconnection coexists with the dayside reconnection. In summary, the features of dayside cusp aurorae and ionospheric convection for the northward and southward IMFs can be seen at different times during the radial IMF event.

# 1. Introduction

The solar wind carries solar magnetic fields into the interplanetary space and forms the interplanetary magnetic field (IMF). In near-earth space, the IMF orientation is typically in the form of an Archimedean spiral. However, in the region where the solar wind velocity decreases gradually or follows an interplanetary coronal mass ejection, a satellite there can observe the direction of an IMF in alignment with (parallel or antiparallel to) the solar wind velocity (Neugebauer & Goldstein, 1997), forming what is best known as the radial IMF. In the present study, we chose a radial IMF event with the duration >1.5 h from the criteria  $|B_x|/B \ge 0.9$  (Pi et al., 2014), where  $B_x$  is the component of the IMF in the direction of the Sun-Earth line and B is the total magnitude of the IMF.

© 2021. American Geophysical Union. All Rights Reserved.

LI ET AL. 1 of 19



Many studies (e.g., Huang et al., 2015; Merka et al., 2003) have revealed that the radial IMF considerably influences the location of the bow shock and magnetopause, causing the bow shock to move closer and the magnetopause further away from the center of the Earth. Under the radial IMF condition, the foreshock moves from dawnside to near noon, and a quasi-parallel shock (shock normal angle less than 45°) forms in front of the bow shock. The plasma can easily cross the bow shock along the field lines and high-speed plasma flows can be observed in the magnetosheath (Plaschke et al., 2013). A characteristic of the magnetosheath jets is higher dynamic pressure than that of that upstream solar wind. In the magnetosheath, a few tens of seconds of antisunward plasma jets were observed (Plaschke et al., 2013), which could deform the magnetopause (Shue et al., 2009).

Auroral luminescence is caused by energetic particles from the magnetosphere moving into the upper atmosphere at high latitudes. From ground-based optical auroral images, their morphology can be divided into discrete and diffuse aurorae. Discrete aurorae are structured and include bands, arcs, and rays. The generation mechanism is related to particle acceleration due to a potential drop along magnetic field line (Christensen et al., 1987). The luminosity of diffuse aurorae is relatively homogenous and lacks any structured pattern (Lui et al., 1973). The discrete auroral arcs exhibited a gap across the midday zone of the auroral oval (Dandekar & Pike, 1978), and intense and structured auroral emission occurred in the morning or afternoon sector. The energy range that creates dayside aurorae for electrons is 100–500 eV, which is lower than that for typical nightside aurorae. The characteristics of the precipitating particles can be used to infer where these particles originate from in the magnetosphere, such as central plasma sheet (CPS), boundary plasma sheet (BPS), low-latitude boundary layer (LLBL), or polar cusp and mantle (Newell & Meng, 1992).

Svalbard, which is located near the northern geomagnetic cusp latitudes, is a prime location for observing dayside cusp aurora. Sandholt, Farrugia, et al. (1998) divided dayside aurora observed at Svalbard into five types, two of which are observed in the cusp at noon, types 1 and 2 aurorae. Type 1 aurora is located within 70°-75° magnetic latitude (MLAT), whereas type 2 aurora forms at slightly higher latitudes, 75°-80° MLAT. Type 1 auroral form is created by the magnetic reconnection process that occurs near the subsolar magnetopause for southward IMF. Type 2 auroral form is associated with lobe reconnection for northward IMF. The electron precipitation related to the type 1 aurora originates from the cusp and frontside LLBL, whereas the particles for the type 2 aurora come from poleward of the cusp and the mantle (Newell & Meng, 1992; Sandholt, Farrugia, et al., 1998). The type 1 aurora is often presented in a poleward-moving auroral form (PMAF; Sandholt, Moen, et al., 1998). PMAF can be a signature of reconnection projected from the magnetospheric boundary layers to the polar ionosphere, such as flux transfer events (FTEs) (Haerendel et al., 1978; Russell & Elphic, 1978), magnetic reconnection (e.g., Øieroset et al., 1997), and magnetic impulse events (Mende et al., 1990). Furthermore, the occurrence of PMAF is not limited to southward IMF (Fasel, 1995). It can also be driven by  $B_{\nu}$ -dominant IMF orientation (Sandholt et al., 2004). Maynard et al. (2001) also indicated that IMF  $B_v$  can establish both dayside and lobe reconnection under strong IMF  $B_v$  condition. As a result, type 1 and type 2 aurora occurred successively. Han et al. (2017) found that the occurrence rate of throat aurora increases with decreasing cone angle of IMF. The throat aurora is analogous to the "crewcuts" form (Rodriguez et al., 2012). The probability of observing throat aurora also increases during quiet geomagnetic periods (Han et al., 2017).

Ionospheric convection is driven by electric fields mapped to the high-latitude ionosphere through solar wind and magnetosphere interactions. The pattern of high-latitude ionospheric convection is determined by the orientation of IMF (e.g., Lockwood, 1991 and *references therein*): Two-cell convection pattern for southward IMF, and four-cell convection pattern for northward IMF. The IMF  $B_y$  can deform the convection pattern, causing the formation of asymmetrical cells in the dawn-dusk direction. During southward IMF, the open magnetic field lines are detected near the dayside magnetopause at the reconnection region between the IMF and the Earth's magnetic field. These open field lines move over the northern and southern cusps and reconnect in the magnetic tail. In the polar ionosphere, plasma drifts over the polar cap in an antisunward direction at noon and then returns back in a sunward direction at the equatorward regions of the auroral oval on the dawnside and duskside, forming the two-cell convection pattern. The convection type is more complicated for the northward IMF. The open magnetic field lines located behind the polar cusp form a four-cell convection pattern under a strong northward IMF condition, and form a three-cell convection pattern under a weak northward IMF condition. The size of their convection cells is smaller than

LI ET AL. 2 of 19



that of convection cells in the southward IMF. Sunward flows can be observed in the polar cap at noon for the northward IMF. Significant antisunward flows near the noon were found under the condition of small IMF  $B_z$  and  $B_y$  components (Kustov et al., 1998). Another type of convection developed on closed field lines is the viscous interaction between the solar wind and magnetosphere (Axford & Hines, 1961), which can contribute to the formation of ionospheric convection at the lower latitude.

In the present study, we examined the auroral and convection patterns obtained from all-sky images and Super Dual Auroral Radar Network (SuperDARN) data in the northern hemisphere for January 4, 2014. The weather conditions of this day enabled us to simultaneously study auroral morphology and convection development under a radial IMF event. In the following sections, we will describe the observational results from the Wind spacecraft, an all-sky camera, the Defense Meteorological Satellite Program (DMSP) satellites, the SuperDARN radar, and the SuperMAG magnetometer. In the Discussion section, we will provide physical explanations for our results. Understanding the responses of the polar cusp to the radial IMF can provide new insight into the magnetosphere-ionosphere coupling in the context of magnetic reconnection.

#### 2. Observations

In this section, we present observations obtained from the Wind spacecraft, an all-sky camera at Svalbard, DMSP's ultraviolet auroral imagers and particle spectrometers, the SuperDARN data, and the SuperMAG magnetometer.

# 2.1. Wind Spacecraft and Its Observations

The Wind spacecraft was deployed at the L1 Lagrange point for collecting the solar wind and IMF data. The Wind spacecraft was located at the geocentric solar magnetic (GSM) coordinates of (196.2, -39.8, -12.6) R<sub>E</sub> at 07:00 UT on January 4, 2014. The 3-s IMF data from the Magnetic Field Investigation (Lepping et al., 1995) and 92-s solar wind data from the Solar Wind Experiment (Ogilvie et al., 1995) were used in this study. Figure 1 presents the solar wind data from the Wind spacecraft during 06:30-09:30 UT. The X, Y, and Z components of the IMF in the GSM coordinates, cone angle, clock angle, dynamic pressure, solar wind velocity, AE index (World Data Center for Geomagnetism, Kyoto et al., 2015), and SYM-H index are displayed from top to bottom. The radial IMF event, which is defined as when the cone angle was below 25°, began at 07:20 UT and ended at 08:55 UT, as delimited by the two black vertical dash lines. The cone angle increased to again exceed 25° during 07:50-07:56 UT, and then dropped below 10° during 08:00-08:23 UT (delimited by the two red vertical dotted lines) even less than 3° (almost purely radial IMF, 08:04–08:16 UT). A southward IMF turning was observed at 08:55 UT with a minimum value of -2.8 nT outside the radial IMF period. Within the interval of the radial IMF, southward IMF could be seen, but its magnitude was small and its duration lasted no more than 10 min. The average values of the  $B_x$ ,  $B_y$ , and  $B_z$  components were -3.79, -0.49, and 0.61 nT, respectively, during the radial IMF interval. The negative  $B_x(B_y)$  component reached a minimum of -4.65 (-2.04) nT at approximately 07:32 (07:54) UT. Dynamic pressure decreased from 07:25 to 07:40 UT. After 08:00 UT, the dynamic pressure remained relatively constant at approximately 1.5 nPa. The average solar wind speed was approximately 490 km/s. The AE and SYM-H indices were used as the indicators of geomagnetic variations. The AE index was less than 50 nT before 08:00 UT and increased to 58 nT from 08:00 to 08:30 UT. The AE index reached the maximum value of 113 nT at 08:49 UT, indicating that a substorm did not occur within the interval of the radial IMF. The values of the SYM-H index varied between -12 and -16 nT, with the mean value being -13 nT.

We estimated the delay time of the IMF effect from the WIND spacecraft to the dayside ionosphere. The delay time was estimated according to the solar wind velocity, and the positions of the bow shock and magnetopause. The positions of the bow shock and magnetopause were calculated using the models developed by Farris and Russell (1994) and Shue et al. (1997), respectively. In terms of error estimation, Suvorova et al. (2010) reported that magnetosphere expansion exceeds model predictions for the radial IMF. We allowed a 10% estimation uncertainty in the positions of the bow shock and magnetopause. The solar wind took  $40 \, (\pm 0.3)$  min to move from the WIND spacecraft to the subsolar bow shock. We assumed that the solar wind speed decreased by a factor of four across the bow shock (Spreiter et al., 1966). The time required for the solar wind to arrive at the magnetopause through the magnetosheath was  $1.3 \, (\pm 0.2)$  min. The transit

LI ET AL. 3 of 19

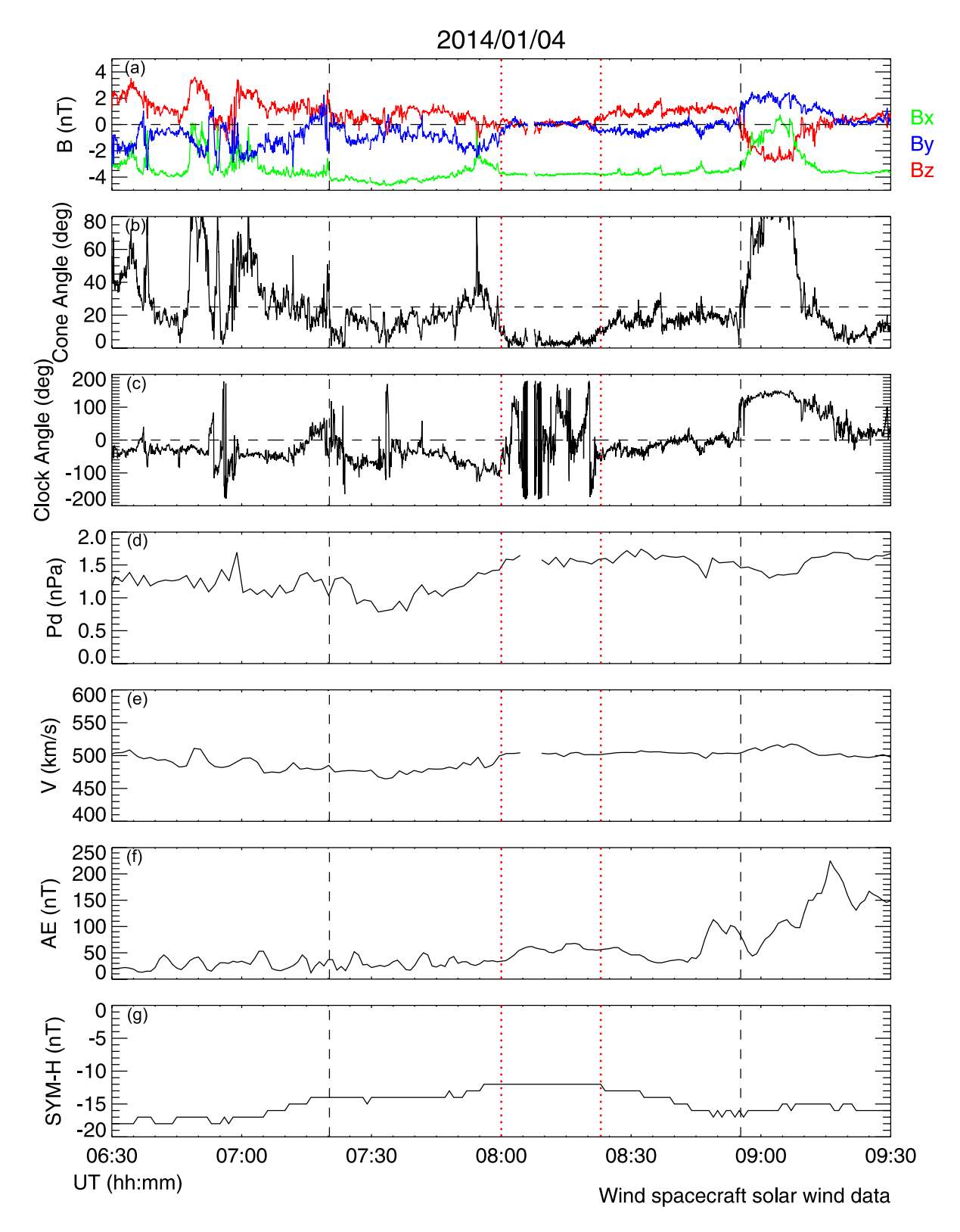


**Figure 1.** Interplanetary magnetic field (IMF) and solar wind conditions measured by the Wind spacecraft. The parameters include (a) the three components (X, Y, and Z) of the IMF in the geocentric solar magnetic (GSM) coordinates, (b) cone angle, (c) clock angle, (d) dynamic pressure, (e) solar wind velocity, (f) the AE index, and (g) the SYM-H index. The radial IMF occurred from 07:20 to 08:55 UT on January 4, 2014, as delimited by the two vertical dash lines. The cone angle was less than 10° from 08:00 to 08:23 UT, as marked by the two red vertical dotted lines. The IMF and solar wind parameters were shifted by 50 min to reflect the time delay from the Wind spacecraft to an effect in the high-latitude ionosphere.

LI ET AL. 4 of 19



time from the magnetopause to the ionosphere as a result of Alfvén propagation was approximately 2 min. As for the time delay in the appearance of ionospheric plasma flows, Øieroset et al. (1997) revealed that sunward flows appeared at noon after approximately 8 min when the IMF was switched from southward to northward. In this study, we assumed that plasma flows (sunward or antisunward flows) would appear at noon with a time delay of  $6(\pm 2)$  min for the radial IMF. The estimated total time delay was between 49 and 53 min. We shifted the solar wind and IMF data with a 50 min delay. Note that this time delay calculation has a limitation because no observations were available at that time to verify the arrival of the radial IMF near the nose of the bow shock. Here we refer to another radial IMF event by Pi et al. (2016) that show a steady propagation of radial IMF. In their event, the magnetic structures of radial IMF just outside the bow shock were not distorted in comparison with the observation at L1. We also examined the magnetic field data of observed by the ACE satellite at 12 MLT and 243 R<sub>E</sub> and those observed by THEMIS-B at 15 MLT and  $58 R_E$  (upstream of the Moon). Their magnetic field data (not shown) still show the existence of radial IMF in the study period, but the magnetic field data of THEMIS-B did not show the feature of almost purely radial IMF. We speculate that, since, the Moon lacks a significant atmosphere and an intrinsic magnetic field, solar wind particles can be absorbed or backscattered to space when they collide with the solid Moon surface. Those particles scattered back into space by the solid Moon can interact with the upstream solar wind, changing the fore-Moon interplanetary magnetic field structure by the diamagnetic current system (e.g., Nishino et al., 2020). Fortunately, the Moon was located at a different side (duskside) from Wind (dawnside) during the event. The IMF observed by Wind, therefore, was least affected by the Moon when arriving near Earth. We calculated the delay time of the solar wind using the flat time-shift method (e.g., Cash et al., 2016) and empirical method (Cameron & Jackel, 2016). We also examined the time shift between the initial appearance of the almost purely radial IMF of the OMNI database and the enhanced antisunward flows of the HAN radar Beam 9. The most likely time delay was ~50 min.

# 2.2. All-Sky Imager and Its Observations

The all-sky imager was equipped with an electron multiplier charge-coupled device camera (Hamamatsu, C9100-13, Hamamatsu, Japan), producing high-resolution auroral images in 512 × 512 pixels with two wavelengths, 557.7 and 630.0 nm. The shooting interval and exposure time for the 630.0 nm emissions set to 4 s. Every 56 s camera change filter to observe 557.7 nm emissions with an exposure time of 2 s (Taguchi et al., 2012). The imager has been in service at Longyearbyen, Svalbard, Norway (geographical latitude 78.1°N, longitude 16.0°E; AACGM-v2 latitude 75.75°N, longitude 110.02°E) since October 2011. The magnetic local time (MLT) of Longyearbyen is calculated as 3 h past universal time. Due to the shooting interval of 630.0 nm emissions, the camera can clearly identify the dynamic nature of the cusp aurora. We also examined images of 557.7 nm emissions for the signature of throat aurora (Han et al., 2015), but this signature was not found in the images for our event. The equatorward edge of the 630.0 nm auroral oval in a keogram can serve as a proxy of the open/closed boundary on the dayside (Milan et al., 1999; Sandholt et al., 1990). Because of the bad weather over Svalbard and strict criteria of radial IMF events, the January 4, 2014 event was the only one for our case study. Figure 2 presents the keogram derived from 557.7 and 630.0 nm all-sky images at Longyearbyen for the event. The auroral intensity increased considerably from 07:44 to 07:48 UT, and increased again from 07:58 to 08:05 UT. Auroral brightness suddenly intensified in the first period (07:44-07:48 UT) and remained at the location between 75.5° and 76.1° MLAT. However, in the second brightening period (07:58-08:02 UT), the main structure of the aurora was moving up approximately 76.7° MLAT. Equatorward- and poleward-moving aurorae occurred from 08:03 to 08:05 UT (Figure 2b). For the temporal and spatial variations of the 630.0 nm of the aurora activities from 07:30 to 08:29 UT, readers are referred to Movie S1 included in the supporting information. The 630.0 nm all-sky images assumed an emission altitude of 250 km (Lockwood et al., 1993) and then mapped to the MLAT-MLT coordinates (Figure 3). The all-sky images for 557.7 nm represent high-energy electrons precipitation ( $E \ge 0.5$  keV, e.g., Maynard et al., 2004) into the ionosphere. Figure 4 displays these images taken from 07:40 to 08:12 UT on January 4, 2014. The emission was assumed to be taken at the altitude of 110 km. Before 07:44 UT, the auroral intensity was weak, as indicated in Movie S1 and Figure 3a. Because of a cloud coverage, the aurora was invisible at 11:45–12:15 MLT (Figure 3a). The brightness of the aurora intensified considerably at 07:44 UT (Figure 3b). At 07:46 UT (Figure 3c), the morphology of the aurora presented a feature of narrow continuous band that concentrated near the zenith. This feature is also shown on the 557.7 nm image (Figure 4c). The auroral

LI ET AL. 5 of 19

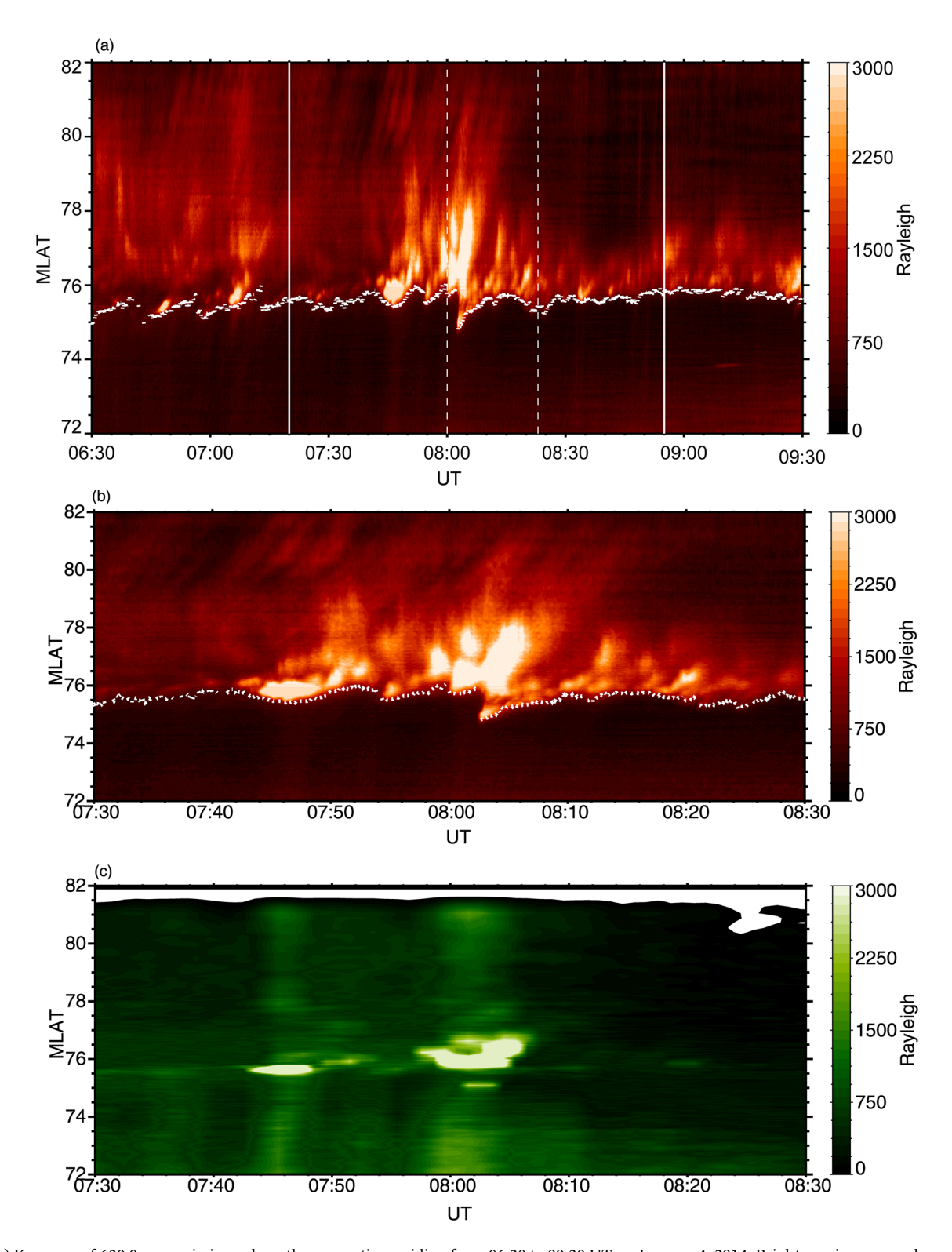


**Figure 2.** (a) Keogram of 630.0 nm emissions along the magnetic meridian from 06:30 to 09:30 UT on January 4, 2014. Brightness is expressed as a function of UT and magnetic latitude in the keogram. The scale for the magnitude of brightness is provided by the color bar on the right. The radial IMF occurred from 07:20 to 08:55 UT on January 4, 2014, as delimited by the two vertical solid white lines. The cone angle was less than 10° from 08:00 to 08:23 UT, as indicated by the two vertical dash white lines. The white irregular zigzag curve represents the variable equatorward boundary of the auroral oval. The equatorward boundary was identified at each column of the keogram from the threshold value of the mean value plus 0.2-times its standard deviation. (b) The zoom-in version of the keogram of 630.0 nm emissions along the magnetic meridian from 07:30 to 08:30 UT on January 4, 2014. (c) The zoom-in version of the keogram of 557.7 nm emissions along the magnetic meridian from 07:30 to 08:30 UT on January 4, 2014.

LI ET AL. 6 of 19

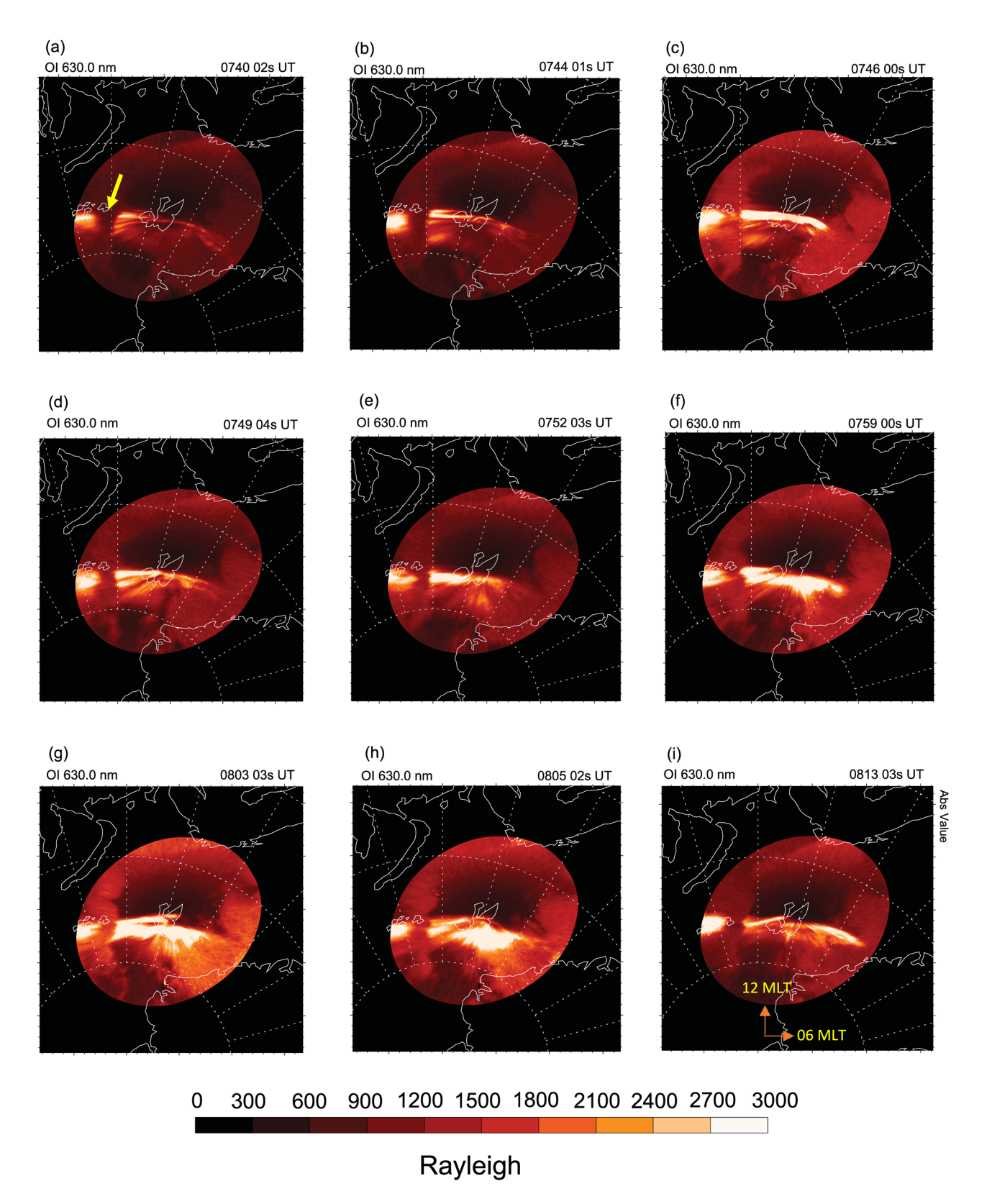


**Figure 3.** Sequence of 630.0 nm images captured by the all-sky imager at Longyearbyen from 07:40 to 08:13 UT on January 4, 2014. (a) Because of cloud (marked by a yellow arrow), the aurora was invisible at the region 11:45–12:15 MLT. (c) At 07:46 UT, the morphology of the aurora presented a feature of narrow continuous band and concentration at the region between 75.5° and 76.1° MLAT. (i) The cusp aurora split near noon (75°–78° MLAT, 10:30–12:00 MLT). The scale for the magnitude of brightness is provided by the color bar on the bottom.

LI ET AL. 7 of 19

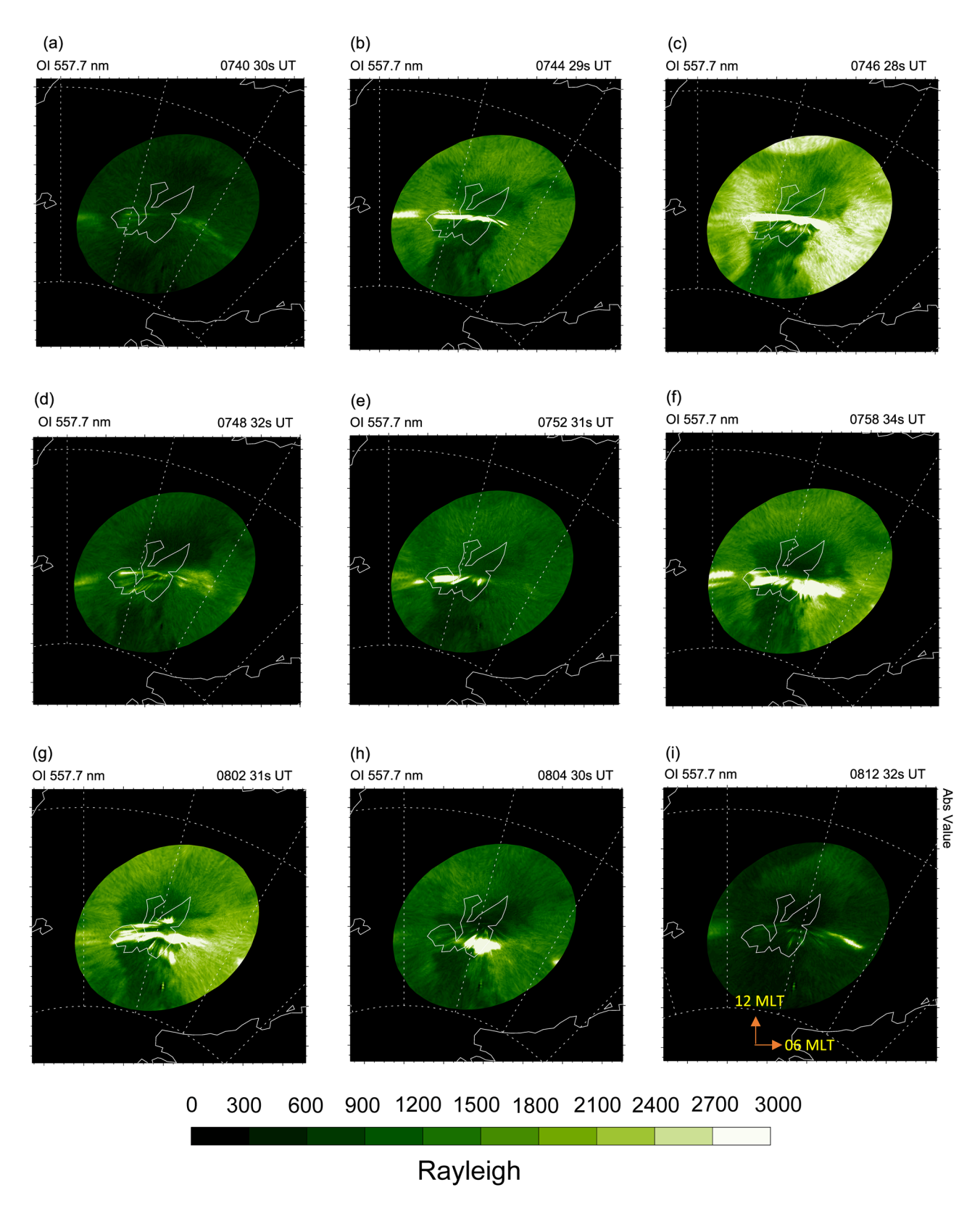


Figure 4. Sequence of 557.7 nm images captured by the all-sky imager at Longyearbyen from 07:40 to 08:12 UT on January 4, 2014. The scale for the magnitude of brightness is provided by the color bar on the bottom.

LI ET AL. 8 of 19



brightness was confined between 75.5° and 76.1° MLAT. This pattern lasted for approximately 5 min and ended at 07:48 UT. After 07:49 UT (Figure 3d), the aurora was no longer a continuous band. In addition to rupturing of the continuous band, a poleward-moving phenomenon appeared from 07:49 to 07:51 UT and an arc emerged at the lower latitude at 07:55 UT (Movie S1). From 07:57 to 07:59 UT, the aurora brightened at approximately 76.5°–77.3° MLAT (Figure 3f) and poleward movement at 07:58 UT (Figure 4f). An arc appears at the lower latitude at 07:59 UT (Movie S1). A "tongue" located at the higher latitude (~77.5° MLAT) of bright band at 11 MLT was found from 08:01 to 08:02 UT (Movie S1). Another arc extends westward at lower latitude from 12 to 11 MLT during 08:01–08:02 UT (Figures 3g and 4g). At 08:03 UT (Figure 3g), the aurora moved much further to the equator; subsequently, a PMAF was observed from the keogram during 08:04–08:06 UT. Figures 3h and 4h show that the cusp aurora split near noon (75°–78° MLAT; 10:30–12:00 MLT) at 08:05 UT and a poleward-moving phenomenon appeared. After 08:08 UT, the aurora splits into the different shape arcs and the brightness are darker than the previous period.

#### 2.3. DMSP Satellites and Their Observations

The DMSP satellites, which operate in a Sun-synchronous orbit, monitor space environments at a typical altitude of 830 km. The Special Sensor Ultraviolet Spectrographic Imager (SSUSI) provides cross-orbital scanning images of the Earth's ultraviolet and far ultraviolet (FUV) auroral emissions, enabling us to monitor the characteristics of aurorae with a global view (Paxton et al., 2002). The SSUSI employs five spectral channels on the image: H Lyman α (121.6 nm), LBHS (N<sub>2</sub> Lyman-Birge-Hopfield short band emission, from approximately 140 to 150 nm), LBHL (N<sub>2</sub> Lyman-Birge-Hopfield long band emission, from approximately 165 to 180 nm), OI (130.4 nm) and OI (135.6 nm). By comparing these bands, we found that the 135.6 nm emission clearly presented the dynamic structure of the aurora. The 135.6 nm emission in the auroral region was mainly produced from excited atomic oxygen from the impact of secondary electrons created by precipitating particles. The particle spectrometers on the DMSP satellite measure ions and electrons energies from 30 eV to 30 keV (Hardy et al., 1984). During the studying period, the three DMSP satellites passed near Svalbard at different times: 07:33 UT (F17), 08:04 UT (F18), and 08:12 UT (F16), one of which (F17) passed directly over Svalbard, although its view did not intersect the main region of interest in the present study. The SSUSI data of F18 was contaminated by unknown reasons on the morning side, we could not use it for this study. Figures 5a and 5b show the particle observations and the 135.6 nm FUV images for the F17 pass. The integral energy flux and average energy of the electrons and ions are arranged in the top two panels, together with the energy fluxes of the electrons and ions in the bottom two panels. The auroral activity was weak (Figure 2a) when F17 passed near the Svalbard area during the period of 07:31-07:34 UT. Since F17 obliquely intersected the main auroral oval and missed right over the Syalbard station during the period, the equatorward boundary of precipitation can only be determined from a comparison of the MLT distribution with Figure 2 of Newell and Meng (1992). Without considering transient behaviors of the aurora, we believe that the precipitation particles observed after 07:33 UT (10:33 MLT) originate from the plasma sheet. The auroral brightness near noon was weak at 07:31 UT (Figure 5b). The S-shaped aurora appeared near noon (75°-78° MLAT; 10:30-12:00 MLT) at 08:13 UT (Figure 5c), which is similar to the auroral structure displayed in Figure 3i.

# 2.4. SuperDARN and Its Observations

The SuperDARN consists of more than 30 low-power high-frequency radars that explore Earth's upper atmosphere from mid-latitude to polar region. The SuperDARN radars continuously transmit and receive radar echoes reflected from the motion of ionospheric irregularities to infer large-scale plasma convection and electric fields in the high-latitude ionosphere (Greenwald et al., 1995). In the standard operation mode, each radar measures the line-of-sight (LOS) velocity of an ionospheric irregularity along 16 beam directions. The coverage region of a radar is approximately 3,500 km in range and approximately 56° in azimuth. The time resolution of a full scan is approximately 1 or 2 min. In this study, we mainly used the ionospheric scatter radar data from Hankasalmi (HAN, Finland) station that has a predominance of the near noon LOS measurements to study the plasma flows of the ionosphere near noon for the radial IMF. Figure 6 illustrates the LOS velocity of the Hankasalmi radar at 07:40, 07:44, 07:46, 07:52, 07:59, 08:03, 08:05, and 08:13 UT, respectively. The red and yellow colors indicate the plasma flowing away from the Hankasalmi radar station

LI ET AL. 9 of 19

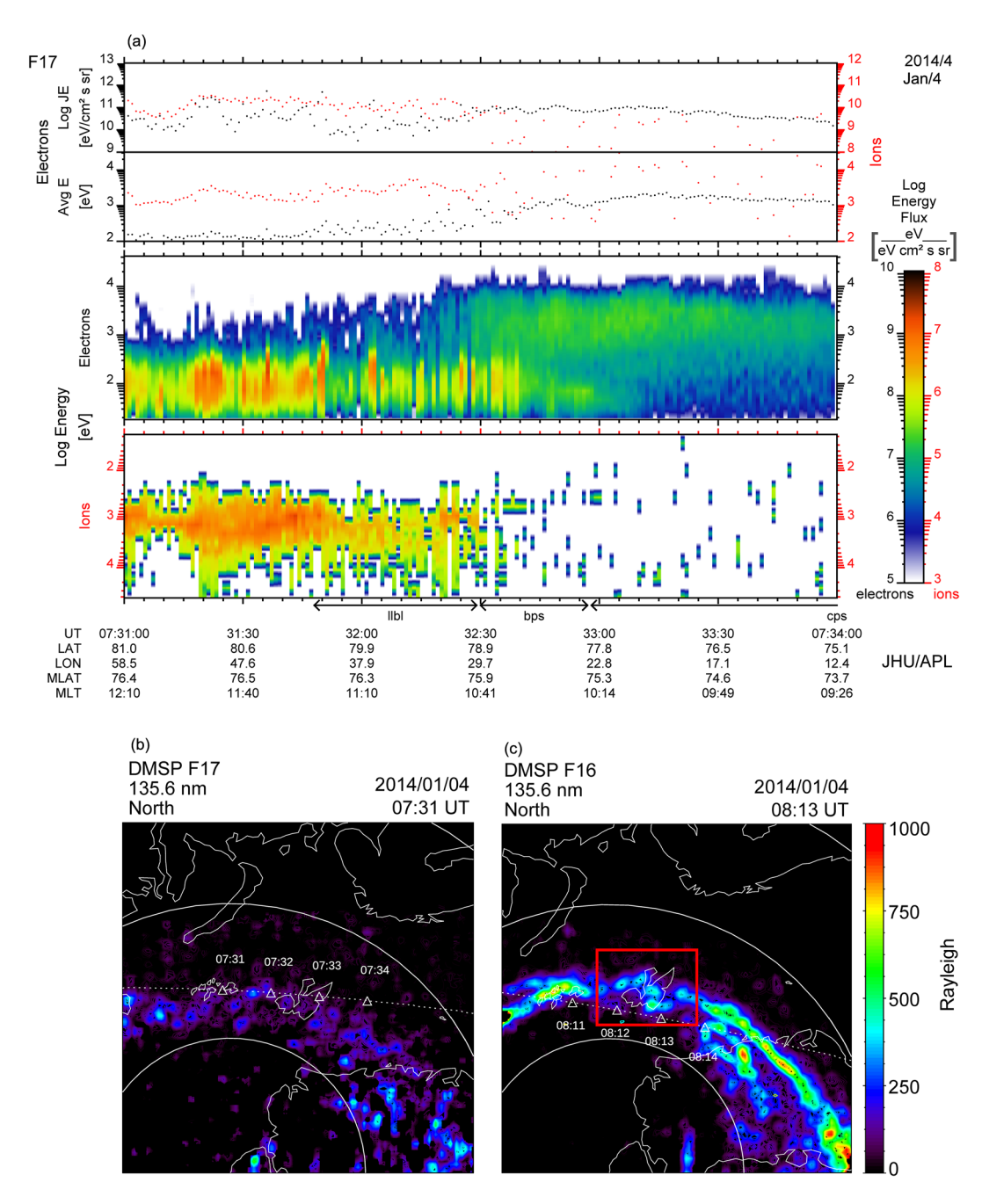


**Figure 5.** Auroral FUV 135.6 nm images captured by the SSUSI and particle observations on board a DMSP satellite between 07:31 and 08:13 UT (satellite orbit apex time) on January 4, 2014. (a) DMSP F17 particle data were observed during the period. The top two panels show the electron and ion integral energy fluxes, and the electron and ion average energy. The bottom two panels present the energy fluxes of the electrons and ions. (b) The FUV image displays weak auroral features near noon (75°–78° MLAT, 10:30–12:00 MLT) at 07:31 UT. (c) The S-shaped auroral structure appeared near noon (75°–78° MLAT, 10:30–12:00 MLT) at 08:13 UT, as marked in the red rectangle. The images are plotted using the MLAT-MLT coordinates.

(poleward direction) along the beam, and the green and blue colors indicate the plasma flowing toward the Hankasalmi radar station (equatorward direction). The coordinates used here are from the MLAT-MLT system, with noon located at the top of each panel. The substantial antisunward flows at noon ( $75^{\circ}-79^{\circ}$  MLAT; 11:30-12:30 MLT) were observed to start at 07:40 UT (Figure 6a). This flow pattern lasted for approximately 4 min until 07:43 UT. From 07:44 to 07:48 UT, antisunward flows (at higher latitudes;  $77^{\circ}-79^{\circ}$  MLAT) and

LI ET AL. 10 of 19

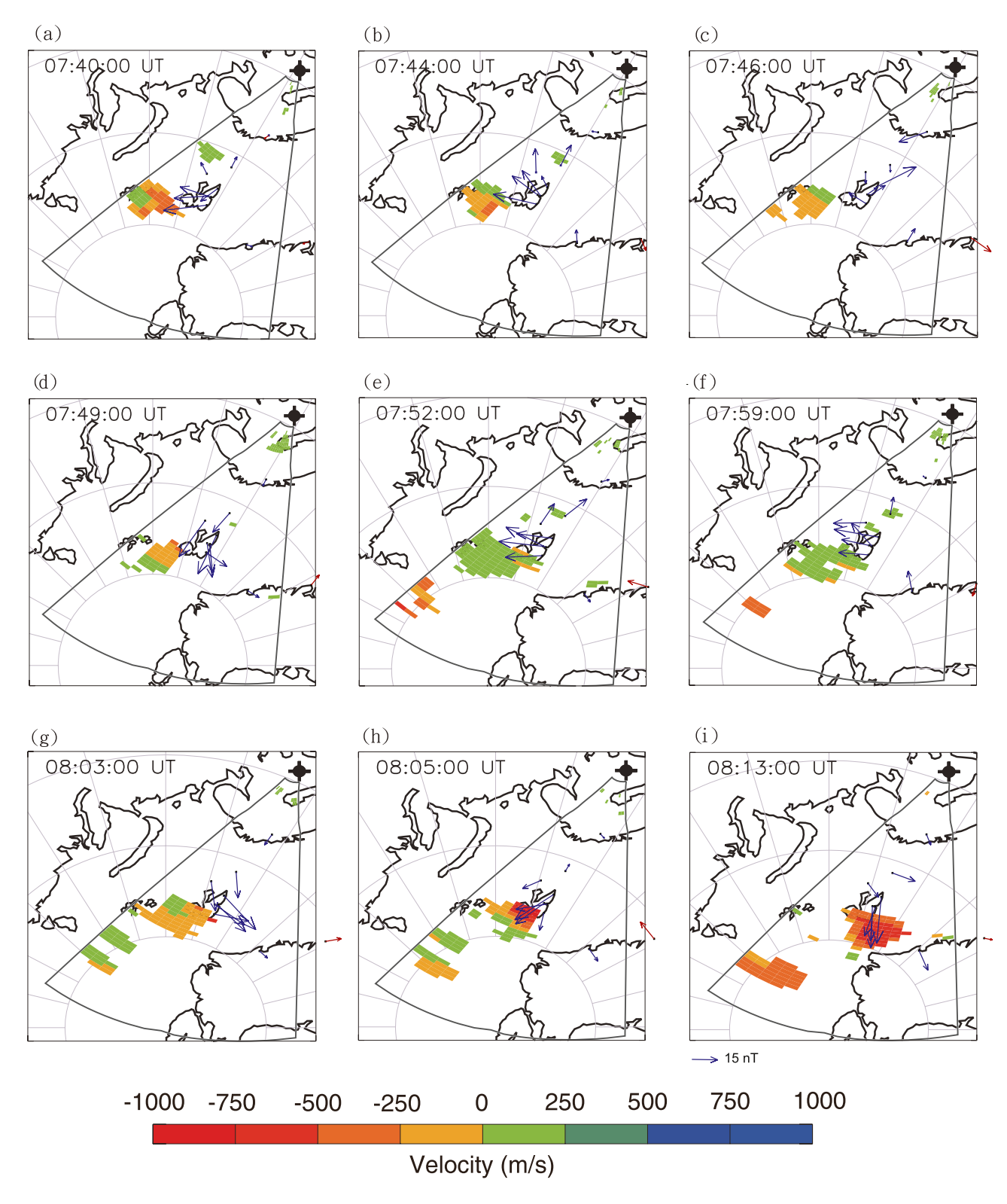


Figure 6. LOS velocities measured using Hankasalmi radar from 07:40 to 08:13 UT on January 4, 2014. The field of view of the radar station is plotted in the fan-shaped region bounded by gray lines and curves. The red and yellow colors represent the velocity of movement away from the radar station along the beam (negative sign), and the green and blue colors represent the velocity of movement toward the radar station (positive sign). The horizontal magnetic field vectors from the SuperMAG magnetometer arrays around the Svalbard, Greenland area, blue arrows, have been rotated 90° anticlockwise to obtain the ionospheric  $E \times B$  drift pattern.

LI ET AL. 11 of 19



sunward flows (at lower latitudes; 75°-77° MLAT) coexisted at noon (07:44 UT; Figure 6b). The locations of antisunward flows (at lower latitudes; 77°-78° MLAT) and sunward flows (at higher latitudes; 78°-79° MLAT) at noon were switched at 07:49 UT (Figure 6d). Sunward flows detected at noon (75°-80° MLAT; 11:00-13:00 MLT) peaked at 07:52 UT (Figure 6e). Thereafter, the sunward flows weakened at 07:53 UT (not shown). From 07:54 to 07:56 UT, antisunward flows appeared again at noon (not shown). At 07:57 UT, the sunward flows appeared at 78°-80° MLAT and the antisunward flows remained at 77°-78° MLAT (not shown). From 07:58 to 08:00 UT (07:59 UT; Figure 6f), the pattern of the sunward flows at noon was similar to that at 07:49-07:53 UT (cf. 07:52 UT; Figure 6e). The antisunward flows were enhanced at 08:01 UT and appeared between 77°-80° MLAT and 11:00-13:00 MLT. The sunward flows were located at 76°-77° MLAT at 08:01 UT. From 08:03 to 08:24 UT (08:03 UT, Figure 6g; 08:05 UT, Figure 6h; 08:13 UT, Figure 6i), the antisunward flows moved to between 76°-80° MLAT and 10:00-11:30 MLT. Afterward, the antisunward flows moved to approximately 10:00 MLT. The plasma flows were too weak to identify the direction during 08:30-08:43 UT (not shown). The antisunward flows at noon developed again from 08:44 to 08:55 UT (not shown). All these observations indicated that antisunward and sunward convection appeared near noon at different times during the radial IMF period (07:20-08:55 UT). Figure 6 also show the SuperMAG magnetic field vectors around the Svalbard, Greenland area on which the quiet-time baselines are removed at 07:40, 07:44, 07:49, 07:52, 07:59, 08:03, 08:05, and 08:13 UT. These horizontal magnetic field vectors, which are marked with blue arrows, have been rotated 90° anticlockwise to show the ionospheric  $E \times B$  drift patterns (e.g., Juusola et al., 2010). The equivalent ionospheric  $E \times B$  drift patterns observed at 08:03, 08:05, and 08:13 UT are consistent with the SuperDARN LOS velocity. The plasma flows began to acquire a poleward component at 08:03 UT and markedly increased the velocity at 08:05 UT. The poleward intensification in velocity continued through 08:13 UT. It should be noted that the coverage of the SuperDARN radar echoes was not spatially coincident for the most part with the magnetometers observing over Svalbard during the event. We think that the inconsistency observed before 08:03 UT is likely related to this dislocation. After 08:03 UT, the received radar echoes were located near the magnetometer station of Svalbard. Both the flow directions well matched to each other, especially a large swing to poleward flows observed at 08:05 and 08:13 UT. Figure 7 shows the backscatter power and LOS Doppler velocities measured on beam 9 of the Hankasalmi radar (near Longyearbyen, Svalbard) during 07:50-08:10 UT. The color scale of the Doppler velocities is the same as that for the convection maps in Figure 6. The plot presents positive (negative) LOS velocities which indicate sunward/equatorward (antisunward/poleward) flows. It shows the general flow direction was not stable during 07:50-08:10 UT. Sunward flows were above 79° MLAT during 07:51-07:54 UT. From 07:54 to 07:57 UT, the antisunward flows occupied the area of beam 9, which is consistent with the poleward motion of the aurora activity shown in Movie S1. At 07:57 UT, the sunward flows appeared at 79°-80° MLAT and the antisunward flows remained at 77°-78° MLAT. At 07:59 UT, the aurora activity shown in Figure 2 demonstrates an equatorward motion, which is consistent with the equatorward convection shown in Figure 7. During 08:02-08:03 UT, sunward flows occurred near the auroral observatory. After 08:03 UT, antisunward flows occurred near the auroral observatory. The blue and red arrows on Figure 7 indicate that the position of LOS Doppler velocity was close to the aurora observatory. The blue arrow indicates that plasma flows had a significant equatorward component at 08:02 UT. Compared to Figure 2, the corresponding auroral activity at about 77.5° MLAT at this time had a tongue shaped feature. The red arrow indicates that flows had a poleward component at 08:05 UT, which is consistent with the poleward-moving aurora activity shown in Figure 2.

#### 3. Discussion

Using auroral images and plasma flow data, we examined the variations of auroral morphology and convection patterns in the polar cap region in the period of radial IMF. We explored the possible mechanisms that control the generation of aurorae and ionospheric convection.

#### 3.1. Auroral Phenomena

Figure 2b shows that the brightness of the aurora did not increase until 07:44 UT during the period of the radial IMF. The aurora considerably increased in brightness during the two periods of 07:44–07:48 and 07:58–08:05 UT. The optical characteristics of the 630.0 and 557.7 nm emission from the first period were confined

LI ET AL. 12 of 19

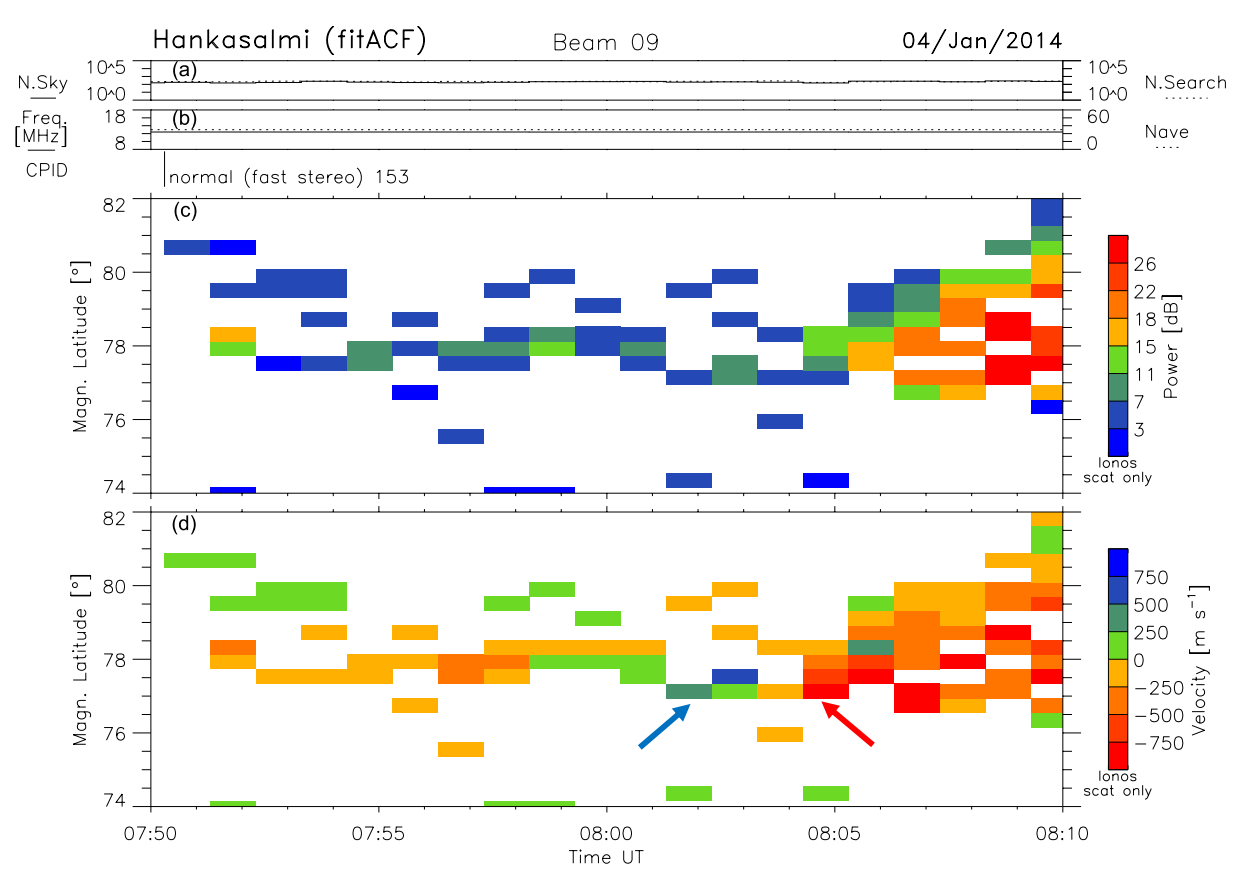


**Figure 7.** The time series plots from beam 9 of the Hankasalmi radar between 07:50 and 08:10 UT on January 4, 2014. (a) The receiver noise, (b) transmitted frequency, (c) backscatter power, and (d) LOS Doppler velocity are displayed from top to bottom. The color scale of the Doppler velocities is the same as that for Figure 6.

near the zenith between 75.5° and 76.1° MLAT. According to its position, the aurora can be classified into the type 2 aurorae (e.g., Sandholt, Farrugia, et al., 1998). The B<sub>z</sub> component of the corresponding IMF was actually positive. However, no plasma flows over Svalbard were observed (Figures 6a-6c). There are two conditions for receiving radar backscatters with a SuperDARN radar. The first is the presence of plasma irregularities. The second is suitable conditions for the HF radar wave propagation. At this time of the year, it is possible that both of these are important, although the lack of irregularities could be the main cause. The all-sky images displayed the morphology of a continuous and uninterrupted band (Figures 3c and 4c). We note that in Movie S1, Figures 3c and 4c, the peak intensity did not spread out substantially, which indicates that precipitation particles along the close field line enter the ionosphere. The auroral morphology and sudden brightening were similar to those in a case studied by Wang et al. (2018), who explained that the aurorae were created by magnetosheath high-speed jets that occur at a high occurrence rate for the radial IMF. On the other hand, the impact of the magnetosheath high-speed jets on the magnetopause has two effects. One is a small-scale distortion by the localized compression over the magnetopause (Shue et al., 2009), resulting in auroral brightness near the cusp (Wang et al., 2018) and the other is a buildup of field-aligned currents near the magnetopause, creating the aurorae in the polar ionosphere (Fujita et al., 2003). Since the DMSP satellite did not cross the bright band at 07:46 UT, we indirectly used a ratio of  $I_{557.7}/I_{630.0}$  to infer the sources of precipitating particles (e.g., Qiu et al., 2017). The  $I_{557.7}/I_{630.0}$  ratio is about 3 for the continuous and uninterrupted band (Figures 3c and 4c). The source of particles may, therefore, come from the plasma sheet. We speculate that the magnetosheath high-speed jets created electron acceleration electric field (e.g., Eriksson et al., 2016) and then the auroral transient at 07:46 UT. However, no data near subsolar magnetosheath during this event were available; therefore, we were unable to verify this speculation.

LI ET AL. 13 of 19



The aurorae moved poleward during 07:49–07:51 UT (Movie S1). The IMF B<sub>v</sub> variations during 07:44–08:01 UT reflected the variable shear angles in references to the magnetopause. Sandholt et al. (2004) reported that the IMF  $B_{\nu}$  affected the evolution of the auroral morphology of poleward moving. In addition, the center of cusp precipitation was longitudinal shifted by the IMF  $B_{\nu}$  (Newell et al., 1989). These precipitation particles entered the ionosphere and altered the morphology of the aurora (such as 07:55 UT; Movie S1). The aurora detected from 07:58 to 07:59 UT also presents a poleward moving feature. The intensity of auroral brightness from 08:00 to 08:02 UT, however, was stronger than that in the previous period, signifying that more particles entered this area and that the aurorae were widely expanded. The solar wind dynamic pressure increased from 0.78 nPa at 07:31 UT to 1.58 nPa at 08:01 UT. The increased dynamic pressure can be balanced by an increase in the magnetic flux of the lobe. The increased lobe pressure roughly enhanced the total pressure of the plasma sheet. As such, the plasma sheet releases energy into the polar cap (e.g., Boudouridis et al., 2003). The auroral transient at 08:01 UT was similar to a bright aurora caused by the enhanced solar wind dynamic pressure. In addition, the plasma flows associated with the "tongue" feature at ~77.5° MLAT had an equatorward motion, which is likely related to lobe reconnection. During 08:01-08:02 UT, the polarity of the  $B_v$  was changed from negative to positive and a lower-latitude auroral arc moved westward and poleward finally, which is likely related to dayside reconnection. The cone angle dropped below 10° during 08:00-08:23 UT even less than 3° (almost purely radial IMF, 08:04-08:16 UT). The charged particles can enter the ionosphere more easily. From 08:01 to 08:05 UT, the keogram (Figure 2b) displays a phenomenon of equatorward and poleward movement. The range-time velocity plot (Figure 7) showed equatorward (blue arrow) and poleward (red arrow) flows on 77.5° MLAT during 08:03-08:05 UT. The movement of aurora on the keogram during 08:01-08:05 UT coincided with the range-time velocity plot. The poleward-moving aurora occurred in the area containing the direction of the tangent to the magnetic field line lines at Longyearbyen, that is, the magnetic zenith at Longyearbyen. The  $I_{557.7}/I_{630.0}$  ratio is approximately 0.2 in the magnetic zenith (~75.1° MLAT, Figures 3h and 4h). This kind of low ratio can be explained as being a result of electrons precipitating along open field lines in the cusp (e.g., Lorentzen & Moen, 2000; Taguchi et al., 2019). The equatorward motion of the open/closed boundary location and PMAF could be linked to magnetic reconnection or FTE that occurred on the magnetopause (Sandholt et al., 1986, 1990). The 557.7 nm data also reflected a similar phenomenon (08:02, 08:04 UT; Figures 4g and 4h). The enhanced 557.7 nm emission can be regarded as a signal of reconnecting on the magnetosphere (e.g., Maynard et al., 2001, 2004). Energetic electrons moving along the open field line at reconnection sites are the sources of 557.7 nm emission. The reconnection between Earth's and interplanetary magnetic field increases 557.7 nm emission brightness. The all-sky image (08:13 UT; Figure 3i) revealed that the morphology of the aurora became irregular arc. The auroral emission on 135.6 nm presented S-shaped at 08:13 UT (Figure 5c), which indicates that the dayside magnetopause might severely deform. Three possible mechanisms causing the magnetopause deformation were the impact of magnetosheath high-speed jets related to the radial IMF (Shue et al., 2009; Wang et al., 2018), local erosion of the magnetopause from magnetic reconnection (e.g., Sibeck, 1994), and a rolled-up structure created from the Kelvin-Helmholtz instability by shear flows on the dayside magnetopause (Grygorov et al., 2016).

We believe that the physical mechanism was different between the two periods of auroral brightness, 07:44–07:48 and 07:58–08:05 UT. The first period was related to the magnetosheath high-speed jet. The second period came from the effect of reconnection and dynamic pressure. On the other hand, the foreshock moved from the dawnside to near noon under the radial IMF condition. The plasma could easily cross the bow shock front along the field lines entering the magnetosphere via magnetosheath high-speed jets. Its influence was reflected in the manifestation of aurora. From Figure 2, aurora had significant activity during 07:44–08:25 UT. The position of foreshock may be a key indicator. As the radial component gradually weakened after 08:30 UT, the foreshock moved back to dawnside subsequently. In addition, the equatorward boundary of the red line aurora is considered to be the open/closed boundary (Johnsen & Lorentzen, 2012; Lorentzen et al., 1996; Taguchi et al., 2015). By evaluating the white zigzag curve shown in the keogram, we find that the footprints of the open/closed boundary changed drastically on small scales during the period of the radial IMF, which indicated an oscillating magnetopause (Suvorova et al., 2010). This phenomenon was particularly noticeable in the cusp where the aurora was particularly bright (07:44–08:10 UT). This interval reflected auroral quasi-periodic movement in the poleward and equatorward directions, which indicates that the magnetic field lines of the magnetopause were intermittently open. Changes in the

LI ET AL. 14 of 19



open/closed boundary also represents relative contributions of particles and energy entering from the solar wind and/or magnetosphere into the high-latitude ionosphere.

#### 3.2. Convection Phenomena

Antisunward or sunward plasma flows were observed in the cusp region, which could be accompanied to PMAFs (e.g., Thorolfsson et al., 2000), FTEs (e.g., Oksavik et al., 2004, 2005), reversed flow events (e.g., Rinne et al., 2007) or throat aurora (Han et al., 2015, 2016). Antisunward flows are created by reconnection on the dayside for the southward IMF, and sunward flows are created by lobe reconnection for the northward IMF. From the SuperDARN convection patterns of this event, the occurrence frequency of antisunward flows at noon was higher than that of sunward flows. When we examined the development of convection during the radial IMF, we observed that the antisunward flows at noon appeared most of the time. However, we also noted evidence of sunward flows that appeared at noon. These two patterns alternately occurred during the period of the radial IMF, that is, when the sunward flows developed at noon, the antisunward flows were suppressed, and vice versa. Moreover, we also observed a short duration of coexisting sunward and antisunward flows in the noon. We believe that the reconnection sites occurred simultaneously on the dayside magnetopause and lobe of the northern hemisphere, which is in accordance with Maynard et al. (2001).

Co-existing sunward and antisunward flows at noon (11:30–12:30 MLT) were observed during the 07:44–07:48 UT, 07:49–07:50 UT, 07:53 UT, 07:57 UT, and 08:01–08:02 UT periods. These two flows alternately occurred during this event, but the duration of coexisting antisunward and sunward flows is short. Maynard et al. (2000, 2001) reported that IMF  $B_y$  bifurcated the reconnection source region. This  $B_y$  effect tilted the dayside magnetopause X line such that the draped IMF encountered new "anti-parallel region" on the geomagnetic field, which means that the variation of the clock angle within a certain range can add the source region of reconnection and increase the reconnection voltage (e.g., Fedder et al., 1991). The short duration may be due to the new anti-parallel region being destroyed by the  $B_y$  tilted effect.

Antisunward flows were enhanced at 08:01 UT and remained stable from 08:05 to 08:23 UT. The locations of the antisunward flows matched those of the aurora on 08:05 UT. The plasma flows over the open/closed boundary indicated an electric field along the reconnected X line at the magnetopause (Vasyliunas, 1984). The IMF clock angle at approximately 08:03 UT was over 100°. When the magnetic shear on the magnetopause is large, the reconnection occurs, consequently creating the electric field across the polar cap (Pudovkin & Semenov, 1985; Sandholt et al., 1996). From 08:03 to 08:05 UT, the keogram displayed an auroral feature of poleward and equatorward movement, which could be linked to magnetic reconnection or flux transfer events. According to the events discussed by Maynard et al. (2000, 2001) and Pi et al. (2017) a dayside reconnection site was located in the southern hemisphere. The stable antisunward flow observed at noon after 08:03 UT can be considered as the evidence of reconnection at the dayside magnetopause (Lockwood & Morley, 2004). Here we note that the radial IMF will eventually evolve into the  $B_y$  or  $B_z$  component just outside the magnetopause because of the draping effect over the magnetosphere. More stable antisunward convection generated in the ionosphere is an indicator of more southward  $B_z$  generated by the draping effect.

Sunward flows at noon were observed in the periods of 07:51–07:52 UT and 07:58–08:00 UT. In those moments, the  $B_z$  component of the IMF was positive, which is consistent with the occurrence of the lobe reconnection for the northward IMF and further northward IMF resulted from a conversion of IMF  $B_x$ . Therefore, the sunward flows at noon developed in the high-latitude ionosphere could suppress the existing antisunward convection. When lobe reconnection in the northern hemisphere stopped, the antisunward flows at noon restored. We also noted that its duration was not as long as that of the antisunward flows. On the basis of this observation, we suggest that the ionospheric convection pattern under the radial IMF generally matched with that under the southward IMF. Unlike the convection for the southward IMF, its intensity was not strong enough. Thus, the convection for the radial IMF could be easily changed by the lobe reconnection.

Hietala et al. (2018) examined magnetosheath high-speed jets observed by THEMIS and reported that they could trigger magnetopause reconnection. It generated a transient response of reconnection during a period

LI ET AL. 15 of 19



of radial IMF. The computer simulation by Tang et al. (2013) revealed that the magnetopause reconnection was present under the radial IMF. We found that the convection was not stable until 08:05 UT, which means that the position of magnetic reconnection was variable in between the lobe and dayside magnetopause. Pi et al. (2016) compared the IMF structure with the magnetic field in the magnetosheath under the radial IMF condition. They showed that the  $B_x$  component of the radial IMF was converted into the other two components, forming an enhanced  $B_z$  component in the magnetosheath. This enhanced  $B_z$  component may extend its direction to further south or north when approaching the magnetopause, creating similar phenomena that resemble the situation for the southward or northward IMFs. That is another possible cause of unstable convection pattern. Here we note that because of a lack of the radial IMF observational evidence just outside the bow shock, it may reduce the validity of the interpretation.

# 4. Conclusions

The major findings of this study included several consequences of magnetic reconnection, such as PMAF, and antisunward/sunward flows, under radial IMF conditions from an analysis of all-sky images and ionospheric convection patterns. We found that PMAF appears during the period of almost purely radial IMF in our event. When we examined the IMF data, no major  $B_z \ll 0$  components were detected. However, the radial IMF could be converted into  $B_z < 0$  in the southern hemisphere and  $B_z > 0$  in the northern hemisphere because of the diverting effect by the magnetosphere (Pi et al., 2017). The negative (positive)  $B_z$  results in the subsolar (lobe) reconnection. Thus, both types of antisunward and sunward convection were observed in the cusp region. When radial IMF close to purely radial state, IMF Bz enhanced the dayside reconnection effect, and the antisunward flows were more stable. On the basis of the magnetospheric configuration by Maynard et al. (2000, 2001) and Pi et al. (2017) and the development of ionospheric convection for the almost purely radial IMF, we suggest that the associated two-cell convection pattern is similar to that of the southward IMF. During the radial IMF, the convection pattern in the polar cap region can become sunward due to lobe reconnection. It also indicates that the strength of the dayside reconnection for the radial IMF is not as strong as that for real southward IMF. The footprints of the open/closed boundary vary drastically in small scales in agreement with auroral morphology observed near the cusp. Based on the results of our analysis, we further suggest that magnetic reconnection in both hemispheres under radial IMF is realistic. However, the duration of the magnetic reconnection is not as long as that for the reconnection by real northward or southward IMF.

# **Data Availability Statement**

The authors would like to thank the Wind spacecraft and science team and T. Iyemori of Kyoto University for providing solar wind data and the SYM-H index through CDAWeb/NASA (https://omniweb.gsfc.nasa.gov), and the World Data Center for Geomagnetism, Kyoto, for providing the *AE* index. Hosokawa's lab in the Department of Communication Engineering and Informatics, University of Electro-Communications provided the all-sky imager movie from their website (http://gwave.cei.uec.ac.jp/cgi-bin/hosokawa/svalcam/svalcam.cgi). Johns Hopkins Applied Physics Laboratory provided the DMSP SSUSI and DMSP SSJ data products through their website (https://ssusi.jhuapl.edu, http://sd-www.jhuapl.edu/Aurora/data-set\_list.html). The authors acknowledge the use of SuperDARN data. The authors also acknowledge the SuperMAG website (http://superMAG.jhuapl.edu) provide the ground magnetometer station data.

# DARN is a **References**

Axford, W. I., & Hines, C. O. (1961). A unifying theory of high-latitude geophysical phenomena and geomagnetic storms. Canadian Journal of Physics, 39(10), 1433–1464. https://doi.org/10.1139/p61-172

Boudouridis, A., Zesta, E., Lyons, R., Anderson, P. C., & Lummerzheim, D. (2003). Effect of solar wind pressure pulses on the size and strength of the auroral oval. *Journal of Geophysical Research*, 108(A4), 8012. https://doi.org/10.1029/2002ja009373

Cameron, T., & Jackel, B. (2016). Quantitative evaluation of solar wind time-shifting methods. Space Weather, 14(11), 973–981. https://doi.org/10.1002/2016SW001451

Cash, M. D., Witters Hicks, S., Biesecker, D. A., Reinard, A. A., de Koning, C. A., & Weimer, D. R. (2016). Validation of an operational product to determine L1 to Earth propagation time delays. Space Weather, 14(2), 93–112. https://doi.org/10.1002/2015SW001321

Christensen, A. B., Lyons, L. R., Hecht, J. H., Sivjee, G. G., Meier, R. R., & Strickland, D. G. (1987). Magnetic field-aligned electric field acceleration and the characteristics of the optical aurora. *Journal of Geophysical Research*, 92(A6), 6163–6167. https://doi.org/10.1029/JA092iA06p06163

#### Acknowledgments

This work was supported by the MOST-108-2111-M-008-019 and MOST-109-2111-M-008-007 grants to the National Central University. SuperDARN is a collection of radars funded by national scientific funding agencies of Australia, Canada, China, France, Italy, Japan, Norway, South Africa, United Kingdom and the United States of America. The authors used the online map velocity tool hosted by the Virginia Tech SuperDARN group on their website (http://vt.superdarn.org/tiki-index. php?page=Map+Velocity+Tool). Mark Lester was supported by STFC grant ST/ S000429/1.

LI ET AL. 16 of 19

- Dandekar, B. S., & Pike, C. P. (1978). The midday, discrete auroral gap. *Journal of Geophysical Research*, 83(A9), 4227–4236. https://doi.org/10.1029/JA083iA09p04227
- Eriksson, E., Vaivads, A., Graham, D. B., Khotyaintsev, Y. V., Yordanova, E., et al. (2016). Strong current sheet at a magnetosheath jet: Kinetic structure and electron acceleration. *Journal of Geophysical Research: Space Physics*, 121(10), 9608–9618. https://doi.org/10.1002/2016JA023146
- Farris, M. H., & Russell, C. T. (1994). Determining the standoff distance of the bow shock: Mach number dependence and use of models. Journal of Geophysical Research, 99(A9), 17681–17689. https://doi.org/10.1029/94JA01020
- Fasel, G. J. (1995). Dayside poleward moving auroral forms: A statistical study. Journal of Geophysical Research, 100(A7), 11891–11905. https://doi.org/10.1029/95JA00854
- Fedder, J. A., Mobarry, C. M., & Lyon, J. G. (1991). Reconnection voltage as a function of IMF clock angle. *Geophysical Research Letters*, 18(6), 1047–1050. https://doi.org/10.1029/90GL02722
- Fujita, S., Tanaka, T., Kikuchi, T., Fujimoto, K., Hosokawa, K., & Itonaga, M. (2003). A numerical simulation of the geomagnetic sudden commencement: 1. Generation of the field-aligned current associated with the preliminary impulse. *Journal of Geophysical Research*, 108(A12), 1416. https://doi.org/10.1029/2002JA009407
- Greenwald, R. A., Baker, K. B., Dudeney, J. R., Pinnock, M., Jones, T. B., Thomas, E. C., et al. (1995). DARN/SuperDARN. Space Science Reviews, 71(1–4), 761–796. https://doi.org/10.1007/BF00751350
- Grygorov, K., Němeček, Z., Šafránková, J., Přech, L., Pi, G., & Shue, J.-H. (2016). Kelvin-Helmholtz wave at the subsolar magnetopause boundary layer under radial IMF. Journal of Geophysical Research Space Physics, 121(10), 9863–9879. https://doi.org/10.1002/2016JA023068
- Haerendel, G., Paschmann, G., Sckopke, N., Rosenbauer, H., & Hedgecock, P. C. (1978). The frontside boundary layer of the magnetosphere and the problem of reconnection. *Journal of Geophysical Research*, 83(A7), 3195–3216. https://doi.org/10.1029/JA083iA07p03195
- Han, D. S., Chen, X. C., Liu, J. J., Qiu, Q., Keika, K., Hu, Z. J., et al. (2015). An extensive survey of dayside diffuse aurora based on optical observations at Yellow River Station. *Journal of Geophysical Research: Space Physics*, 120(9), 7447–7465. https://doi.org/10.1002/2015JA021699
- Han, D. S., Chen, X. -C., Nishimura, X. C., Lyons, L. R., Liu, J. -J., et al. (2017). Observational properties of dayside throat aurora and implications on the possible generation mechanisms. *Journal of Geophysical Research: Space Physics*, 122(2), 1853–1870. https://doi.org/10.1002/2016JA023394
- Han, D.-S., Nishimura, Y., Lyons, L. R., Hu, H.-Q., & Yang, H.-G. (2016). Throat aurora: The ionospheric signature of magnetosheath particles penetrating into the magnetosphere. *Geophysical Research Letters*, 43(5), 1819–1827. https://doi.org/10.1002/2016GL068181
- Hardy, D. A., Schmidt, L. K., Gussenhoven, M. S., Marshall, F. J., Yeh, H. C., Shumaker, T. L. et al. (1984). Precipitating electron and ion detectors (SSJ/4) for block 5D/flights 4–10 DMSP satellites: Calibration and data presentation. *Tech Rep AFGL-TR-84-0317*, Air Force Geophys Lab, Hanscom Air Force Base, Mass.
- Hietala, H., Phan, T. D., Angelopoulos, V., Oieroset, M., Archer, M. O., Karlsson, T., & Plaschke, F. (2018). In situ observations of a magnetosheath high-speed jet triggering magnetopause reconnection. *Geophysical Research Letters*, 45(4), 1732–1740. https://doi. org/10.1002/2017GL076525
- Huang, T., Wang, H., Shue, J.-H., Cai, L., & Pi, G. (2015). The dayside magnetopause location during radial interplanetary magnetic field periods: Cluster observation and model comparison. *Annales Geophysicae*, 33(4), 437–448. https://doi.org/10.5194/angeo-33-437-2015
- Johnsen, M. G., & Lorentzen, D. A. (2012). A statistical analysis of the optical dayside open/closed field line boundary. *Journal of Geophysical Research*, 117(A2). https://doi.org/10.1029/2011JA016984
- Juusola, L., Andréeová, K., Amm, O., Kauristie, K., Milan, S. E., Palmroth, M., & Partamies, N. (2010). Effects of a solar wind dynamic pressure increase in the magnetosphere and in the ionosphere. Annales Geophysicae, 28(10), 1945–1959. https://doi.org/10.5194/angeo-28-1945-2010
- Kustov, A. V., Lyatsky, W. B., & Sofko, G. J. (1998). Super Dual Auroral Radar Network observations of near-noon plasma convection at small interplanetary magnetic field  $B_z$  and  $B_y$ . Journal of Geophysical Research, 103(A3), 4041–4050. https://doi.org/10.1029/97JA03457
- Lepping, R. P., Acūna, M. H., Burlaga, L. F., Farrell, W. M., Slavin, J. A., Schatten, K. H., et al. (1995). The WIND magnetic field investigation. Space Science Reviews, 71(1-4), 207–229. https://doi.org/10.1007/BF00751330
- Lockwood, M. (1991). The excitation of ionospheric convection. *Journal of Atmospheric and Terrestrial Physics*, 53(3–4), 177–199. https://doi.org/10.1016/0021-9169(91)90103-E
- Lockwood, M., Carlson, H. C., & Sandholt, P. E. (1993). Implications of the altitude of transient 630-nm dayside auroral emissions. *Journal of Geophysical Research*, 98(A9), 15571–15587. https://doi.org/10.1029/93JA00811
- Lockwood, M., & Morley, S. K. (2004). A numerical model of the ionospheric signatures of time-varying magnetic reconnection: I. ionospheric convection. *Annales Geophysicae*, 22(1), 73–91. https://doi.org/10.5194/angeo-22-73-2004
- Lorentzen, D. A., Deehr, C. S., Minow, J. I., Smith, R. W., Stenbaek-Neielsen, H. C., Sigernes, F., et al. (1996). SCIFER-Dayside auroral signatures of magnetospheric energetic electrons. *Geophysical Research Letters*, 23(14), 1885–1888. https://doi.org/10.1029/2020GL09 211910.1029/96gl00593
- Lorentzen, D. A., & Moen, J. (2000). Auroral proton and electron signatures in the dayside aurora. *Journal of Geophysical Research*, 105(A6), 12733–12745. https://doi.org/10.1029/1999JA900405
- Lui, A. T. Y., Perreault, P., Akasofu, S.-I., & Anger, C. D. (1973). The diffuse aurora. Planetary and Space Science, 21(5), 857–861. https://doi.org/10.1016/0032-0633(73)90102-5
- Maynard, N. C., Burke, W. J., Pfaff, R. F., Weber, E. J., Ober, D. M., Weimer, D. R., et al. (2000). Driving dayside convection with northward IMF: Observations by a sounding rocket launched from Svalbard. *Journal of Geophysical Research*, 105(A3), 5245–5263. https://doi.org/10.1029/1999JA900462
- Maynard, N. C., Burke, W. J., Sandholt, P. E., Moen, J., Ober, D. M., Lester, M., et al. (2001). Observations of simultaneous effects of merging in both hemispheres. *Journal of Geophysical Research*, 106(A11), 24551–24577. https://doi.org/10.1029/2000JA0031510.1029/2000ja000315
- Maynard, N. C., Moen, J., Burke, W. J., Lester, M., Ober, D. M., Scudder, J. D., et al. (2004). Temporal-spatial structure of magnetic merging at the magnetopause inferred from 557.7-nm all-sky images. *Annales Geophysicae*, 22(8), 2917–2942. https://doi.org/10.5194/angeo-22-2917-2004
- Mende, S. B., Rairden, R. L., Lanzerotti, L. J., & Maclennan, C. G. (1990). Magnetic impulses and associated optical signatures in the day-side aurora. *Geophysical Research Letters*, 17(2), 131–134. https://doi.org/10.1029/GL017i002p00131
- Merka, J., Szabo, A., Šafránková, J., & Němeček, Z. (2003). Earth's bow shock and magnetopause in the case of a field-aligned upstream flow: Observation and model comparison. *Journal of Geophysical Research*, 108(A7), 1269. https://doi.org/10.1029/2002JA009697

LI ET AL. 17 of 19



- Milan, S. E., Lester, M., Cowley, S. W. H., Moen, J., Sandholt, P. E., & Owen, C. J. (1999). Meridian-scanning photometer, coherent HF radar, and magnetometer observations of the cusp: A case study. *Annales Geophysicae*, 17(2), 159–172. https://doi.org/10.1007/s00585-999-0159-5
- Neugebauer, M., & Goldstein, R. (1997). Particle and field signatures of coronal mass ejection in the solar wind. In N. Crooker, J. A. Joselyn, & J. Feynman (Eds.), Coronal mass ejections, geophysical monograph series (Vol. 99, pp. 245–251). American Geophysical Union. https://doi.org/10.1029/GM099p0245
- Newell, P. T., & Meng, C.-I. (1992). Mapping the dayside ionosphere to the magnetosphere according to particle precipitation characteristics. *Geophysical Research Letters*, 19(6), 609–612. https://doi.org/10.1029/92GL00404
- Newell, P. T., Meng, C.-I., Sibeck, D. G., & Lepping, R. (1989). Some low-altitude cusp dependencies on the interplanetary magnetic field. Journal of Geophysical Research, 94(A7), 8921–8927. https://doi.org/10.1029/JA094iA07p08921
- Nishino, M. N., Saito, Y., Tsunakawa, H., Harada, Y., Takahashi, F., Yokota, S., et al. (2020). Decrease of the interplanetary magnetic field strength on the lunar dayside and over the polar region. *Icarus*, 335, 113392. https://doi.org/10.1016/j.icarus.2019.113392
- Ogilvie, K. W., Chornay, D. J., Fritzenreiter, R. J., Hunsaker, F., Keller, J., Lobell, J., et al. (1995). SWE, A comprehensive plasma instrument for the wind spacecraft. Space Science Reviews, 71(1-4), 55-77. https://doi.org/10.1007/BF00751326
- Øieroset, M., Sandholt, P. E., Denig, W. F., & Cowley, S. W. H. (1997). Northward interplanetary magnetic field cusp aurora and high-latitude magnetopause reconnection. *Journal of Geophysical Research*, 102(A6), 11349–11362. https://doi.org/10.1029/97JA00559
- Oksavik, K., Moen, J., & Carlson, H. C. (2004). High-resolution observations of the small-scale flow pattern associated with a poleward moving auroral form in the cusp. *Geophysical Research Letters*, 31(11), L11807. https://doi.org/10.1029/2004GL019838
- Oksavik, K., Moen, J., Carlson, H. C., Greenwald, R. A., Milan, S. E., Lester, M., et al. (2005). Multi-instrument mapping of the small-scale flow dynamics related to a cusp auroral transient. *Annales Geophysicae*, 23(7), 2657–2670. https://doi.org/10.5194/angeo-23-2657-2005
- Paxton, L. J., Morrison, D., Zhang, Y., Kil, H., Wolven, B., Ogorzalek, B. S., et al. (2002). Validation of remote sensing products produced by the Special Sensor Ultraviolet Scanning Imager (SSUSI): A far UV-imaging spectrograph on DMSP F-16. Optical Spectroscopic Techniques, Remote Sensing, and Instrumentation for Atmospheric and Space Research IV, 4485, 338–348. https://doi.org/10.1117/12.454268
- Pi, G., Shue, J.-H., Chao, J.-K., Němeček, Z., Šafránková, J., & Lin, C.-H. (2014). A reexamination of long-duration radial IMF events. *Journal of Geophysical Research: Space Physics*, 119(9), 7005–7011. https://doi.org/10.1002/2014JA019993
- Pi, G., Shue, J.-H., Grygorov, K., Li, H.-M., Němeček, Z., Šafránková, J., et al. (2017). Evolution of the magnetic field structure outside the magnetopause under radial IMF conditions. *Journal of Geophysical Research: Space Physics*, 122(4), 4051–4063. https://doi. org/10.1002/2015JA021809
- Pi, G., Shue, J.-H., Park, J.-S., Chao, J.-K., Yang, Y.-H., & Lin, C.-H. (2016). A comparison of the IMF structure and the magnetic field in the magnetosheath under the radial IMF conditions. Advances in Space Research, 58(2), 181–187. https://doi.org/10.1016/j.asr.2015.11.012
- Plaschke, F., Hietala, H., & Angelopoulos, V. (2013). Anti-sunward high-speed jets in the subsolar magnetosheath. *Annales Geophysicae*, 31(10), 1877–1889. https://doi.org/10.5194/angeo-31-1877-2013
- Pudovkin, M. I., & Semenov, V. S. (1985). Magnetic field reconnection theory and the solar wind? Magnetosphere interaction: A review. Space Science Reviews, 41(1–2), 1–89. https://doi.org/10.1007/BF00241346
- Qiu, Q., Yang, H.-G., Lu, Q.-M., & Hu, Z.-J. (2017). Correlation between emission intensities in dayside auroral arcs and precipitating electron spectra. Chinese Journal of Geophysics, 60(1), 1–11. https://doi.org/10.1002/cjg2.30023
- Rinne, Y., Moen, J., Oksavik, K., & Carlson, H. C. (2007). Reversed flow events in the winter cusp ionosphere observed by the European Incoherent Scatter (EISCAT) Svalbard radar. *Journal of Geophysical Research*, 112(A10), A10313. https://doi.org/10.1029/2007JA012366
- Rodriguez, J. V., Carlson, H. C., & Heelis, R. A. (2012). Auroral forms that extend equatorward from the persistent midday aurora during geomagnetically quiet periods. *Journal of Atmospheric and Solar-Terrestrial Physics*, 86, 6–24. https://doi.org/10.1016/j.jastp.2012.06.001
- Russell, C. T., & Elphic, R. C. (1978). Initial ISEE magnetometer results: Magnetopause observations. Space Science Reviews, 22(6), 681–715. https://doi.org/10.1007/BF00212619
- Sandholt, P. E., Deehr, C. S., Egeland, A., Lybekk, B., Viereck, R., & Romick, G. J. (1986). Signatures in the dayside aurora of plasma transfer from the magnetosheath. *Journal of Geophysical Research*, 91(A9), 10063–10079. https://doi.org/10.1029/JA091iA09p10063
- Sandholt, P. E., Farrugia, C. J., & Denig, W. F. (2004). Dayside aurora and the role of IMF |B<sub>y</sub>|/|B<sub>z</sub>|: Detailed morphology and response to magnetopause reconnection. *Annales Geophysicae*, 22(2), 613–628. https://doi.org/10.5194/angeo-22-613-2004
- Sandholt, P. E., Farrugia, C. J., Moen, J., & Lybekk, B. (1998). The dayside aurora and its regulation by the interplanetary magnetic field. In J. Moen, A. Egeland, & M. Lockwood (Eds.), *Polar Cap Boundary Phenomena* (pp. 189–208). Springer. https://doi.org/10.1007/978-94-011-5214-3 15
- Sandholt, P. E., Farrugia, C. J., Stauning, P., Cowley, S. W. H., & Hansen, T. (1996). Cusp/cleft auroral forms and activities in relation to ion-ospheric convection: Responses to specific changes in solar wind and interplanetary magnetic field conditions. *Journal of Geophysical Research*, 101(A3), 5003–5020. https://doi.org/10.1029/95JA03126
- Sandholt, P. E., Lockwood, M., Oguti, T., Cowley, S. W. H., Freeman, K. S. C., Lybekk, B., et al. (1990). Midday auroral breakup events and related energy and momentum transfer from the magnetosheath. *Journal of Geophysical Research*, 95(A2), 1039–1060. https://doi.org/10.1029/JA095iA02p01039
- Sandholt, P. E., Moen, J., Stauning, P., Holtet, J. A., Cowley, S. W. H., Lockwood, M., et al. (1998). Temporal and spatial variability of auroral forms in the 10-14 MLT sector: Relationship to plasma convection and solar wind-magnetosphere coupling. *Earth, Planets and Space*, 50(8), 663–682. https://doi.org/10.1186/BF03352161
- Shue, J.-H., Chao, J. K., Fu, H. C., Russell, C. T., Song, P., Khurana, K. K., & Singer, H. J. (1997). A new functional form to study the solar wind control of the magnetopause size and shape. *Journal of Geophysical Research*, 102(A5), 9497–9511. https://doi.org/10.1029/97JA00196
- Shue, J.-H., Chao, J.-K., Song, P., McFadden, J. P., Suvorova, A., Angelopoulos, V., et al. (2009). Anomalous magnetosheath flows and distorted subsolar magnetopause for radial interplanetary magnetic fields. Geophysical Research Letters, 36(18). L18112. https://doi.org/10.1029/2009GL039842
- Sibeck, D. G. (1994). Signatures of flux erosion from the dayside magnetosphere. *Journal of Geophysical Research*, 99(A5), 8513–8529. https://doi.org/10.1029/93ja03298
- Spreiter, J. R., Summers, A. L., & Alksne, A. Y. (1966). Hydromagnetic flow around the magnetosphere. *Planetary and Space Science*, 14(3), 223–253. https://doi.org/10.1016/0032-0633(66)90124-3
- Suvorova, A. V., Shue, J. -H., Dmitriev, A. V., Sibeck, D. G., McFadden, J. P., Hasegawa, H., et al. (2010). Magnetopause expansions for quasi-radial interplanetary magnetic field: THEMIS and Geotail observations. *Journal of Geophysical Research*, 115(A10). A10216. https://doi.org/10.1029/2010ja015404
- Taguchi, S., Hosokawa, K., & Ogawa, Y. (2015). Investigating the particle precipitation of a moving cusp aurora using simultaneous observations from the ground and space. *Program in Earth and Planet Science*, 2, 11. https://doi.org/10.1186/s40645-015-0044-7

LI ET AL. 18 of 19



10.1029/2019JA027664



- Taguchi, S., Hosokawa, K., & Ogawa, Y. (2019). Plasma flow in the north-south aligned discrete aurora equatorward of the cusp. *Journal of Geophysical Research: Space Physics*, 124(12), 10778–10793. https://doi.org/10.1029/2019JA026895
- Taguchi, S., Hosokawa, K., Ogawa, Y., Aoki, T., & Taguchi, M. (2012). Double bursts inside a poleward-moving auroral form in the cusp. Journal of Geophysical Research, 117(A12), A12301. https://doi.org/10.1029/2012JA018150
- Tang, B. B., Wang, C., & Li, W. Y. (2013). The magnetosphere under the radial interplanetary magnetic field: A numerical study. *Journal of Geophysical Research: Space Physics*, 118(12), 7674–7682. https://doi.org/10.1002/2013JA019155
- $Thorolfsson, A., Cerisier, J.-C., Lockwood, M., Sandholt, P. E., Senior, C., \& Lester, M. (2000). Simultaneous optical and radar signatures of poleward-moving auroral forms. \\ \textit{Annales Geophysicae}, 18 (9), 1054–1066. \\ \text{https://doi.org/10.1007/s00585-000-1054-2}$
- Vasyliunas, V. M. (1984). Steady state aspects of magnetic field line merging. In E. W. Hones (Ed.), Magnetic Reconnection in Space and Laboratory Plasmas (pp. 25–31). American Geophysical Union. https://doi.org/10.1029/gm030p0025
- Wang, B., Nishimura, Y., Lyons, L., Angelopoulos, V., Plaschke, F., et al. (2018). Impacts of magnetosheath high-speed jets on the magnetosphere and ionosphere measured by optical imaging and satellite observations. *Journal of Geophysical Research: Space Physics*, 123(6), 4879–4894. https://doi.org/10.1029/2017JA024954
- World Data Center for Geomagnetism, Kyoto, N. M., Iyemori, T., Sugiura, M., & Kamei, T. (2015). Geomagnetic AE index. https://doi.org/10.17593/15031-54800

LI ET AL. 19 of 19